LARGE EDDY SIMULATION OF A SUPERSONIC PLASMA FLOW OVER A BACKWARD FACING STEP

Kenji Miki, Joey Schulz, and Suresh Menon
Georgia Institute of Technology
Atlanta, GA, 30332-0150, USA
kenji-miki@aerospace.gatech.edu

ABSTRACT

A large-eddy simulation (LES) model using a local dynamic kinetic energy model (LDKM) for closure is used to investigate the effect of applied magnetic and electric fields on the flow development in a supersonic step-combustor. The magnetohydrodynamic (MHD) equations are solved numerically using a finite volume method with a multi-state approximate MHD Riemann solver to compute the fluxes. The resistive fluxes in the magnetic induction equation are determined using an analytical approximation in order to relax the time-step constraint. The results show the capability of external fields to control and/or change supersonic shear flow and their potential for mixing and combustion enhancement.

INTRODUCTION

The important issues that still need to be addressed in the design of feasible scramjets are mixing enhancement and flame stabilization, especially at high combustor inlet Mach numbers. A wide variety of "passive" geometrical enhancements have been proposed to overcome these difficulties. While these approaches do provide some enhancement, plasma-assisted combustion may offer a more versatile design with the potential for increased performance. However, there are many unresolved issues including the exact nature of how the plasma effect can be introduced at the requisite location to manipulate fuel-air mixing. Furthermore, although there is some experimental evidence (Meyer et al., 2003) that plasma source in a fuel rich stream can be an effective source of free radicals (which then can enhance and stabilize combustion), there is no numerical prediction of this effect. The current effort is directed toward addressing these unresolved issues.

Supersonic flow over a rearward facing step is a classical configuration that has been used effectively as a flame holder in scramjet combustor. Fuel injection from just upstream of the step, from the base, and in the recirculation region are all being explored as means for efficient fuel-air mixing strategy in this device. Electrical discharges and applied magnetic fields have also been considered by many authors for enhancement. Leonov and Yarantsev (2006) numerically and experimentally investigated the effect of a variety of electrical discharges on scramjet combustion. Khan and Hoffmann (2006) have investigated the effects of MHD in the low magnetic Reynolds number limit and showed that an applied magnetic field near the step increases the distance from the step where reattachment occurs as a result of increased pressure in the recirculation region.

Our previous work demonstrated the ability of an electrical discharge to affect the flow properties of a turbulent shear layer (Schulz et al., 2006). A non-equilibrium, 11 species kinetic model was used to simulate the plasma source. This previous approach, however, was limited to low magnetic Reynolds number. In another recent study, a LES approach using a LDKM closure model for the subgrid gas kinetic energy and magnetic energy has also been developed (Miki and Menon, 2006).

The current model is designed to be robust and versatile for a large number of applications. Thus, no limiting assumptions are made, and the MHD equations are solved in a conservative fashion using an upwind finite volume scheme. Solution to the MHD Riemann problem is obtained using a multi-state approximate Riemann solver. The non-ideal magnetic terms in the MHD equations are computed in order to account for Ohmic heating and magnetic diffusion in plasmas with finite resistivity.

NUMERICAL FORMULATION

Governing Equations

An electrically conducting fluid is governed by the MHD equations. This set of equations consists of an equation for the time evolution of the magnetic field and the usual unsteady, compressible, Navier-Stokes equations but with additional magnetic terms in the momentum and energy equations (Freton *et al.*, 2000). By applying a spatial (Favre) filter to these equations, the variables can be decomposed into resolved and unresolved parts. The spatial filter width is the local grid scale $\overline{\Delta}$, and the density weighted filtered variables are defined by $\widetilde{f} = \overline{\rho f}/\overline{\rho}$, where $\overline{\ast}$ signifies spatial averaging. The resulting filtered LES equations are (Menon and Patel, 2006):

$$
\begin{cases}
\frac{\partial \bar{\rho}}{\partial t} + \frac{\partial}{\partial x_j}(\bar{\rho}\tilde{u}_j) = 0 \\
\frac{\partial \bar{\rho}\tilde{u}_i}{\partial t} + \frac{\partial}{\partial x_j}\left(\bar{\rho}\tilde{u}_i\tilde{u}_j + \bar{p}\delta_{ij} - \bar{\tau}_{ij} - \bar{T}_{ij} + \tau_{ij}^{sgs} + T_{ij}^{sgs}\right) = 0 \\
\frac{\partial \bar{\rho}\tilde{E}}{\partial t} + \frac{\partial}{\partial x_i}\left[\left(\bar{\rho}\tilde{E} + \bar{p}\right)\tilde{u}_i - \bar{\kappa}\frac{\partial \bar{T}}{\partial x_i} - \tilde{u}_j\bar{\tau}_{ij} - H_i^{sgs} - \sigma_i^{sgs,v}\right] \\
\quad = \frac{\bar{J}_k\bar{J}_k}{\sigma} + \tilde{u}_i\frac{\partial \bar{T}_{ij}}{\partial x_j} - \bar{R}_d + \frac{5k_b}{2q}\left(\frac{\bar{J}_j}{c_p}\frac{\partial \bar{T}}{\partial x_j}\right) + O^{sgs} \\
\frac{\partial \bar{B}_i}{\partial t} + \frac{\partial}{\partial x_j}\left(\tilde{u}_j\bar{B}_i - \bar{B}_j\tilde{u}_i + \tau_{ij}^{sgs,b} - \bar{\lambda}\frac{\partial \bar{B}_i}{\partial x_j} - d_j^{sgs,b}\right) = 0 \\
\bar{p} = \bar{\rho}R\bar{T}
\end{cases}
$$

Here ρ, u_i, p, R and T are density, velocity, pressure, gas constant, and temperature, respectively. In the momentum equation, τ_{ij} is the viscous stress tensor and T_{ij} is magnetic stress tensor defined as:

$$
\frac{\partial T_{ij}}{\partial x_j} = \epsilon_{ijk}J_jB_k = \frac{\partial}{\partial x_j}\left\{\frac{B_iB_j}{\mu_0} - \frac{B_kB_k}{2\mu_0}\delta_{ij}\right\} \tag{1}
$$

Here, ϵ_{ijk} is the alternating tensor, J_i is the current density, B_i is the magnetic field and μ_0 is the magnetic
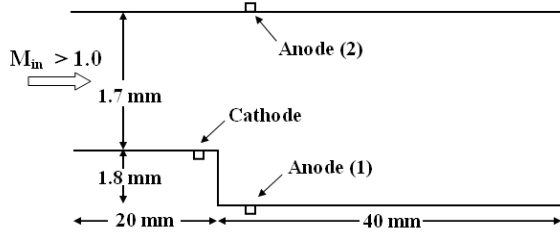
Figure 1: Schematic of the dump combustor. The physical size is similar to the experimental set up by Hartfield (1993). The location of the cathode and the two anodelocations (labelled Configuration 1 and 2) are also shown.

Figure 2: Density profile of the one-dimensional shock tube test.

permeability. The magnetic stress tensor, T_{ij} is analogous to the viscous stress tensor having both shear stress and pressure terms. In the energy equation, E is the sum of the kinetic and internal energies, κ is the thermal conductivity, k_b is Boltzmann's constant, c_p is the specific heat, and q is the electronic charge. The electrical heat flux is divided into two terms: a resistive heating term and a work term. If the Hall effect is ignored, the resistive heating term simplifies to the first term on the right-hand side of the energy equation. The second term on the right-hand side represents the energy expended in Lorentz acceleration. R_d represents the energy lost to radiation, and the last term reflects the energy transfer due to electron mobility in an electric field. In the induction equation, λ is the magnetic diffusivity [$\lambda = (\sigma \mu_0)^{-1}$], where σ is the electric conductivity.

When external fields are applied, it is convenient to solve for the scalar electric potential and the vector magnetic potential. The total magnetic field in the above governing equations is the sum of the applied external field and the time-varying magnetic field. Similarly, the total current density appearing in the energy equation is the sum of the external current resulting from the application of an electric field and the time-varying current density. The external magnetic field and the current density are calculated, respectively, from the scalar and the vector potentials as: $\bar{B}_{ex,i} = \epsilon_{ijk} \frac{\partial \bar{A}_k}{\partial x_j}$, $\bar{J}_{ex,i} = -\bar{\sigma} \frac{\partial \bar{\phi}}{\partial x_i}$. Here, $\bar{A}_k$ is the vector potential of magnetic field and $\bar{\phi}$ is the electric potential. These are calculated by solving the following equation in addition to the LES equations (Patankar, 1980; Freton *et al.* , 2000):

$$\frac{\partial \bar{\rho}\bar{Q}}{\partial t} = \frac{\partial}{\partial x_i}\left(\bar{\Gamma}\frac{\partial \bar{Q}}{\partial x_i}\right) + S \qquad (2)$$

where $\bar{Q} = \bar{A}_k$ or $\bar{\phi}$. $\bar{\Gamma}$ is the diffusion coefficient, which is unity for A_k and $\bar{\sigma}$ for ϕ (Freton *et al.* , 2000). S is the source term and is $\mu_0 \bar{J}_{ex,i}$ for $\bar{A}_k$ and zero for $\bar{\phi}$.

Closure of subgrid terms.
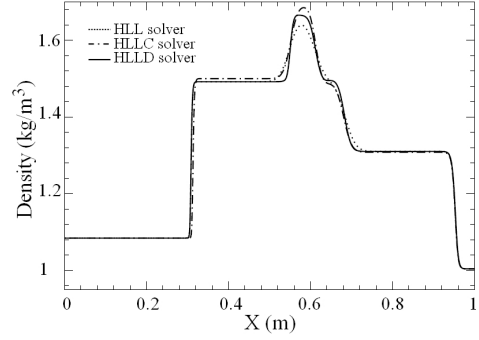
The subgrid terms appearing in the above LES equations

are defined as:

$$
\begin{cases}
\tau_{ij}^{sgs} = \bar{\rho}\widetilde{u_i u_j} - \bar{\rho}\tilde{u}_i \tilde{u}_j \\
T_{ij}^{sgs} = \frac{\overline{B_i B_j} - \bar{B}_i \bar{B}_j}{\mu_0} - \left(\frac{\overline{B_k B_k} - \bar{B}_k \bar{B}_k}{2\mu_0}\right)\delta_{ij} \\
H_{ij}^{sgs} = (\bar{\rho}\widetilde{Eu_i} - \bar{\rho}\tilde{E}\tilde{u}_i) + \overline{pu_i} - \bar{p}\tilde{u}_i \\
\sigma_{ij}^{sgs,v} = \widetilde{u_i \tau_{ij}} - \tilde{u}_i \bar{\tau}_{ij} \\
\tau_{ij}^{sgs,b} = (\overline{u_j B_i} - \overline{u_i B_j}) - (\tilde{u}_j \bar{B}_i - \tilde{u}_i \bar{B}_j) \\
d_j^{sgs,b} = \overline{\lambda \frac{\partial B_i}{\partial x_j}} - \bar{\lambda}\frac{\partial \bar{B}_i}{\partial x_j} \\
O^{sgs} = \frac{\overline{J_k J_k}}{\sigma} - \frac{\bar{J}_k \bar{J}_k}{\bar{\sigma}} + u_i \widetilde{\frac{\partial T_{ij}}{\partial x_j}} - \tilde{u}_i \frac{\partial \bar{T}_{ij}}{\partial x_j} \\
+ \frac{5k_b}{2q}\left(\overline{\frac{J_j}{c_p}\frac{\partial T}{\partial x_j}}\right) - \frac{5k_b}{2q}\left(\frac{\bar{J}_j}{c_p}\frac{\partial \bar{T}}{\partial x_j}\right)
\end{cases}
$$

In the current model, O^{sgs} is neglected. The validity of this assumption remains uncertain. The other terms are modeled using the subgrid kinetic energy [$k^{sgs} = \frac{1}{2}(\widetilde{u_k u_k} - \tilde{u}_k \tilde{u}_k)$] and the subgrid magnetic energy [$k^{sgs,b} = \frac{1}{2\mu_0}(\overline{B_k B_k} - \bar{B}_k \bar{B}_k)$]. The assumption that subgrid dynamics at the grid cutoff scale are similar to the smallest resolved scale (test-scale) allows the determination of the subgrid terms (Menon and Patel, 2006). The advantage of using the kinetic and magnetic energy invariants over other invariants, such as the helicity (Yoshizawa and Yokoi, 1996), is that the governing equations for k^{sgs} and $k^{sgs,b}$ are simpler and require fewer modeling coefficients. Most importantly, the LDKM removes the necessity of *ad hoc* procedures that many other MHD turbulence models require (Miki and Menon, 2006).

The MHD-LDKM governing equations for k^{sgs} and $k^{sgs,b}$ are given as:

$$
\begin{cases}
\frac{\partial \bar{\rho}k^{sgs}}{\partial t} + \frac{\partial}{\partial x_i}\bar{\rho}k^{sgs}\tilde{u}_i = \frac{\partial}{\partial x_i}\left(\bar{\rho}\frac{\nu_e}{Pr_t}\frac{\partial k^{sgs}}{\partial x_i}\right) - \tau_{ij}^{sgs}\frac{\partial \tilde{u}_j}{\partial x_i} \\
\qquad\qquad - T_{ij}^{sgs}\frac{\partial \tilde{u}_j}{\partial x_i} - \frac{\bar{\rho}C_\epsilon}{\triangle}(k^{sgs})^{\frac{3}{2}} \\
\frac{\partial k^{sgs,b}}{\partial t} + \frac{\partial}{\partial x_i}(\tilde{u}_i k^{sgs,b}) = -k^{sgs,b}\frac{\partial \tilde{u}_i}{\partial x_i} + \frac{\partial}{\partial x_k}(\bar{\lambda}\frac{\partial k^{sgs,b}}{\partial x_k}) \\
\qquad\qquad - \frac{1}{\mu_0}\tau_{ij}^{sgs,b}\frac{\partial \bar{B}_i}{\partial x_j} - \frac{C_{\epsilon,b}}{\triangle\sqrt{\bar{\rho}}}(k^{sgs,b})^{\frac{3}{2}}
\end{cases}
$$

where $C_{\epsilon,b}$, C_ϵ are dynamically calculated using LDKM. Both equations have the same forms with transport, production, diffusion, and dissipation terms. More details about the closure of these terms can be found in (Menon and Patel, 2006; Miki and Menon, 2006).

MHD Riemann Solver

A Godunov-type finite volume method is employed here. The accuracy of such a scheme relies on an exact or approximate solution to the Riemann problem. Exact solutions to both the gas dynamic and MHD Riemann problem are
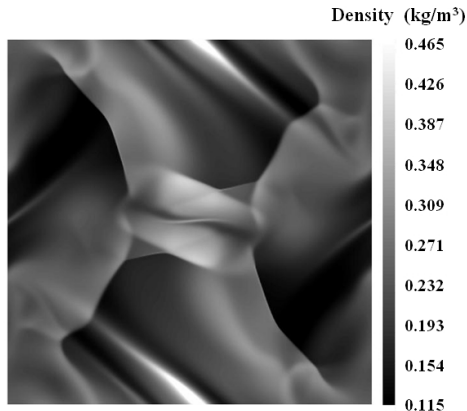
Figure 3: Density contour for Orszag-Tang vortex problem using the HLLC scheme at a 400×400 grid resolution at t=0.5 s.
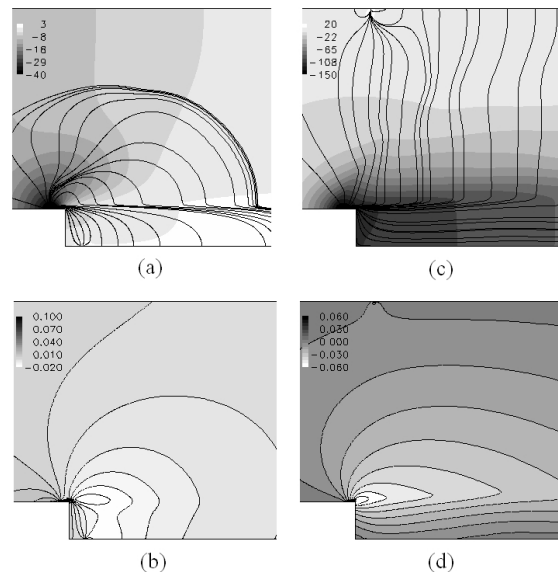

Figure 4: (a) Electric potential contours [V] and current (black lines) contours for configuration (1) and (b) magnetic contours [T] for configuration (1). Similarly, configuration (2) is shown in (c) and (d).

tedious, expensive, and often unnecessary. As a result, several approximate solutions to the the Riemann problem have been developed. The approximate Riemann solver devised by Harten, Lax, and van Leer (HLL) (1983), and the class of approximate Riemann solvers that have followed their development removes the necessity of wave decomposition and also have the property of being positively conservative with the appropriate choice of wave speeds. Gurski (2004) and Li (2005) have attempted to extend the HLLC framework of Toro (1997) to the MHD equations (here the 'C' indicates that the contact wave is being resolved). Miyoshi (2005) has developed a four-state approximate Riemann solver called HLLD for the ideal MHD equations. The accuracy of the HLLD scheme is improved by removing the assumption that the components of the magnetic field are constant across the Riemann fan by incorporating the two Alfven waves.

Several of these numerical methods have been implemented in our study: the HLL and HLLC schemes for MHD and the HLLD scheme. These schemes solve the ideal MHD equations in a conservative fashion. The non-ideal terms in the magnetic induction and the energy conservation equations result from the plasma having finite resistivity. The fluxes associated with these resistive terms and the corresponding viscous terms are determined outside the framework of the Riemann problem. Upwind values of the primitive variables determined from the Riemann solver are used to approximate the viscous and the resistive fluxes, which are then combined with the ideal fluxes obtained from the Riemann solver. The species concentrations are treated as passive scalars, and it is assumed that both the subgrid kinetic energy and the subgrid magnetic energy act as passive scalars.

It is well known that these equations have seven eigenvalues corresponding to the two fast magnetoacoustic waves, the two slow magnetoacoustic waves, the two Alfven waves, and the entropy wave. The two fast magneto-acoustic waves bound the Riemann fan in the MHD problem. It is obvious that when the magnetic field is zero the seven waves collapse to hydrodynamic case of the two acoustic waves and the one entropy wave. Thus, the HLLC solver for hydrodynamics is included within the MHD HLLC and HLLD solvers in the limit of zero magnetic field.

The HLL-type of approximate Riemann solvers assume that the characteristic speeds of the waves that separate the "averaged" states can be determined. To determine these characteristic speeds exactly would require an exact solution to the Riemann problem. Here, we approximate these wave speeds only from initial data using the algorithm proposed by Einfeldt *et al.* (1991) to estimate the left and the right velocities that bound the Riemann problem. This approach has been proven to be extremely robust and gives the exact velocity for isolated discontinuities. This algorithm requires estimating the Roe-average for the normal velocity and the bounding signal speeds. The Roe-averaged fast magneto-acoustic wave speed and normal velocity are obtained using the approach presented by Cargo and Gallice (1997).

A Riemann problem is constructed at the interface of each cell and takes as inputs left and right interface values. In order to increase the accuracy of the scheme, the cell-centered primitive values can be linearly extrapolated to determine the left and the right states at the interface. Conservative values could also be extrapolated. This increases the spatial resolution of the scheme from first order to nominally second order. It is well known, however, that high-order reconstruction schemes produce un-physical oscillations in the vicinity of large gradients. In order to limit these oscillations, a slope limiting approach, known as the Monotone Upstream-Centered Scheme for Conservation Laws (MUSCL) method is employed. Several limiter options are available. The monotized-central (MC) slope limiter is used in this paper (Toro, 1997).

A one-dimensional shock-tube test case is first performed. The initial conditions are given by $(\rho, p, u, v, w, B_y, B_z) = (1.08, 0.95, 1.2, 0.01, 0.5, 3.6f, 2f)$ for $x < 0$ and $(\rho, p, u, v, w, B_y, B_z) = (1, 1, 0, 0, 0, 4f, 2f)$ for $x > 0$ with $B_x = 4f$, with the conversion factor, $f = 1/\sqrt{4\pi}$. The solution consists of two fast shocks, two rotational discontinuities, two slow shocks, and one contact discontinuity. The results are presented in Fig. 2. As expected, both the HLLD and the HLLC schemes resolve the contact discontinuity while the rotational discontinuities are smeared out by the HLLC scheme as a result of the assumption that the magnetic field is constant over the Riemann fan.
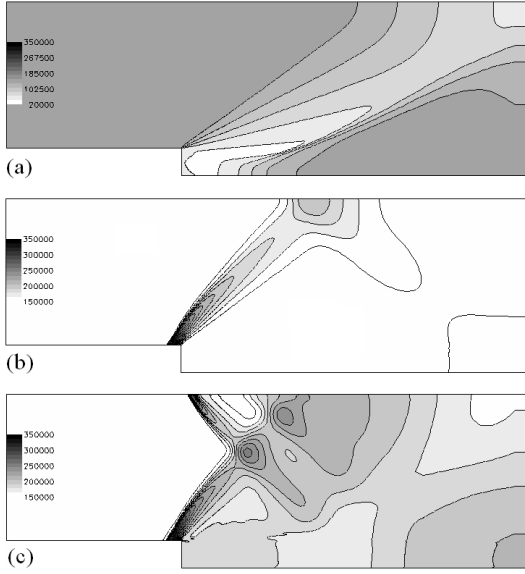
Figure 5: Pressure distribution [Pa] (a) No electrical field, (b) Anode at the bottom wall, and (c) Anode at the top wall.

The extension of the one-dimensional MHD-type solvers to multi-dimensions is not straight-forward and is complicated because the solenoidal constraint of the magnetic field is no longer satisfied numerically. Several multi-dimensional schemes have been developed in the past to reduce the divergence error. The method of flux constrained transport is used in this paper. A comprehensive discussion of this method and many others is given by Gabor (2000)

The Orszag-Tang vortex problem is routinely used as a two-dimensional test for MHD schemes. The initial conditions of the problem are given by $(\rho, p, u, v, w, B_x, B_y, B_z) = (\rho_0, p_0, -\sin 2\pi y, \sin 2\pi x, 0.0, -\sin 2\pi y, \sin 4\pi x, 0.0)$ in a domain $0.0 < x, y < 1.0$. The constants ρ_0 and p_0 are determined as in Dai and Woodward (1998) by $\beta_0 = p_0/(|B|^2/8\pi) = 8\pi p_0$ and $M_0 = \rho_0/\gamma p_0$. In this example, $\beta_0 = 10/3$ and $M_0 = 1.0$ are used. Periodic boundary conditions are imposed on all boundaries. Figure 3 shows the density at $t = 0.5$ seconds using the HLLC solver (Li, 2005). The results are in good agreement with past predictions.

Boundary Conditions for the Scramjet

For the scramjet studies, on all solid surfaces, the no-slip, adiabatic conditions are imposed, except at the cathode and the anode surfaces, which are held at a constant temperature of $T_{wall} = 3500\ K$ (Freton *et al.*, 2000). At the solid surfaces, and at the inlet and the outlet, the scalar potential, $\bar{\phi}$ and the vector potential, $\bar{\mathbf{A}}$ are required to have zero normal gradients. This translates to requiring $\frac{\partial \bar{\phi}}{\partial n_i} = 0$ and $\frac{\partial \bar{A}_i}{\partial n_i} = 0$, where n_i is the surface normal unit vector. At the anode and the cathode surfaces an analytical form, commonly used in the literature (Hsu *et al.*, 1982; Freton *et al.*, 2000), is used to specify the current density distribution, and is given by: $\bar{J}_{ex,y}(l) = J_{max} exp(-bl)$, where J_{max} and b are the constant, and l is the distance from the center of cathode. In our model, $J_{max} = 1.4 \times 10^8\ Am^{-2}$ for the 200 A case, and b is set to 2000 by calculating the total current. The estimated size of electric nodes is $\approx 0.5\ mm$.

Diffusion Model

An explicit time-integration is used in the current study. This approach limits the time-step to the slowest physical process. The magnetic Prandtl number varies by several orders of magnitude throughout the simulation. The time-step is limited by the diffusion processes within the relatively small region of high magnetic field intensity near the cathode and the anode surfaces. Typical characteristic time scales for the different physical mechanism are : viscous diffusion: $\Delta t_{d,\mu_e} \approx 10^{-5}s$, convection: $\Delta t_c \approx 10^{-8}s$, thermal diffusion: $\Delta t_{d,\bar{\kappa}} \approx 10^{-9}s$, electric diffusion: $\Delta t_{d,\bar{\sigma}} \approx 10^{-9} \sim 10^{-12}s$, and magnetic diffusion: $\Delta t_{d,\bar{\lambda}} \approx 10^{-12} \sim 10^{-15}s$. If the smallest time-step is chosen, it would be $\approx 10^{-15}s$. Such a small time step reduces the feasibility of the simulation. An implicit scheme could be used, however, updating the field quantities as each time step can be computationally very expensive. Moreover, since the variation of temperature (and electrical conductivity) is significant, solving $\frac{\partial \bar{\sigma}}{\partial x_i} \frac{\partial \bar{\phi}}{\partial x_i} + \bar{\sigma} \frac{\partial^2 \bar{\phi}}{\partial x_i^2} = 0$ is numerically unstable. Another approach is to use a dual time-stepping method. In this method, the diffusion flux is calculated $N_{\bar{\sigma}}$ times during a single flow time step, where $N_{\bar{\sigma}}$ is determined by $N_{\bar{\sigma}} = \Delta t_c/\Delta t_{d,\bar{\sigma}}$. Typical values of $N_{\bar{\sigma}}$ for this application are $N_{\bar{\sigma}} \simeq 100 \sim 1000$. This method is still restricting, since the time scales of Δt_c and $\Delta t_{d,\bar{\lambda}}$ are different by more than six orders of magnitude.

Thus, to remove these stringent time-step constraints, the diffusion of the magnetic field is modeled using an approximate analytical expression. To determine the diffusion flux at each interface of two adjacent cells x_i and x_{i+1}, a total of four cell-centered points are used to approximate the profile of the local magnetic field. If the boundary points are referenced at zero, a simple analytical solution exists.

$$B(x, t) = \sum_{n=0}^{n=\infty} D_n \left(sin \frac{n\pi x}{L} \right) exp \left(-\frac{n^2 \pi^2 \bar{\lambda} t}{L^2} \right) \quad (3)$$

where

$$D_n = \frac{2}{L} \int_0^L f(x) sin \frac{n\pi x}{L} dx \quad (4)$$

Here, $f(x)$ is the initial profile at $t = 0$, and L is the length between x_{i-1} and x_{i+2}. Using this expression, the magnetic diffusion flux during Δt_c is obtained by:

$$Flux = \int_0^{\Delta t_c} \bar{\lambda} \frac{\partial B(x, t)}{\partial x} dt \quad (5)$$

For validation of this method, we compare magnetic field profiles obtained from the approximated analytical expression given above and from a traditional finite difference solution. The overall agreement is good.

NUMERICAL RESULTS

For current study, the gas is assumed to be pure Argon since the transport coefficients, such as the electrical conductivity, the viscosity, and the thermal conductivity are all well known values. The thermal properties such as the specific heat are easily calculated, and the radiation loss terms can be approximated. Curve-fits for these quantities can be found in literature (Evans and Hawley, 1967).

For all cases, the following incoming flow conditions are used: $U_{in} = 1000\ ms^{-1}$ $(M_{in} = 1.7)$, $P_{in} = 1.4 \times 10^5\ Pa$, and $T_{in} = 1000\ K$. In the cases investigated below, either the applied magnetic field or the applied current is held constant throughout the simulation time.
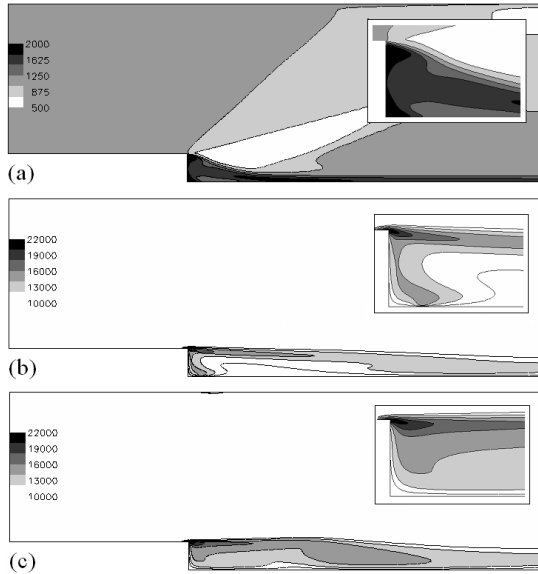
Figure 6: Temperature distribution [K] (a) No electric field,
(b) Anode at the bottom wall, (c) Anode at the top wall.

Applied Electric Field

An electric field is applied in the rearward-facing step by
prescribing a potential difference between two conducting
surfaces (the cathode and the anode). Two different config-
urations are investigated. The cathode is mounted on the
bottom wall just before the step in both configurations, and
only the location of the anode is varied; for the first config-
uration, the anode is located on the bottom wall aft of the
step, and for the second configuration, the anode is located
on the top wall. Figures 4(a)-(d) show the distributions of
the electric field, the current lines, and the magnetic field
for these two configurations.

Figures 5(a) and 6(a) show the pressure and the temper-
ature distributions, respectively, for the nominal case with
no applied external fields. Several well known features are
captured here, including the expansion fan at the corner
which creates a low pressure recirculating region just aft of
the step. The temperature also decreases and reaches a min-
imum of approximately $500\ K$. The inlet boundary layer on
the wall separates at the corner and the resulting free shear
layer bends downward as a result of the low pressure re-
circulating region, eventually reattaching at the lower wall
further downstream. A recompression shock is seen as the
shear layer attaches to the wall.

When an electric field is applied in either of the configu-
rations, the most noticeable difference is that no expansion
fan forms at the corner of the step. This is obvious from the
pressure distribution profiles for these two cases given in Fig.
5(b) and Fig. 5(c). Instead, a strong shock is formed just
prior to the electrical discharge surfaces. In configuration
(1), (Fig. 5(b)), only one shock is formed, since the anode
is located in the recirculation zone. However, in configura-
tion (2), (Fig. 5(c)), two oblique shocks are created, which
merge together in the center of the flow. The reason these
shocks develop is that the high temperature region near the
electrical discharge surfaces act as bluff bodies. The large
thermal gradient in these regions promote boundary layer
separation and the formation of the oblique shocks. As a re-
sult of the shock waves, the downstream velocity is reduced,
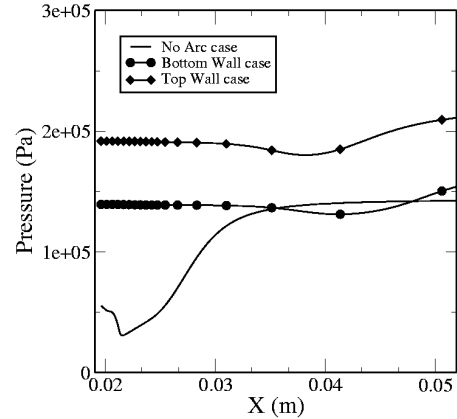especially for configuration (2) as a result of the formation

Figure 7: Pressure profile along the bottom wall behind the
step.

of two oblique shocks.

Figures 6(b) and 6(c) show temperature profiles for con-
figurations (1) and (2), respectively. Since, the temperature
is relatively large when the field is tuned on, the color map
has been rescaled for case of zero applied field. Since the flow
has a finite resistivity, the flow is not only accelerated as a
result of both thermal and magnetic forces, but also heats
up significantly as a result of resistive electrical heating. For
either configuration, since the current is held constant, the
maximum temperature is approximately $(22,000\ K)$, which
is significantly higher than the case with no applied field.
Since large temperature gradients exist when an electric field
is applied, thermal expansion occurs in the vicinity of the
corner. This thermal expansion coupled with the Lorentz
force keeps the shear layer from bending downward and reat-
taching at the lower wall.

Figure 7 represents pressure distribution along the bot-
tom wall. In comparison with the non-arc case, the two
cases with the arc have flat profiles and there is no grad-
ual pressure increase seen for the non-arc case, which occurs
due to recompression shock. It is clear that there is no reat-
tachment of shear layer. For configuration (2), the pressure
is twice as large as the other configurations because of the
merging of the two shock waves. Furthermore, it can be seen
that the pressure gradually increases downstream when an
electric field is applied. This is related to the approach of
the shear layer to the bottom wall.

A possible mechanism by which the plasma can affect
turbulent shear flow is by changing the local vorticity field.
As shown earlier (Schulz et al., 2006), a possible mecha-
nism is the modification of the baroclinic torque by the local
plasma source. The profile of the magnitude of baroclinic
torque defined as $(\nabla \bar{P} \times \nabla \bar{\rho})/\bar{\rho}^2$ and the Mach number are
shown in Figs. 8(a)-(b). The applied electric field creates
large temperature and density gradients, which increases the
magnitude of the baroclinic torque. Since the baroclinic
torque term acts as aaproduction term for turbulence, the
flow is expected to be highly turbulent within the shear layer.
This may aid in the enhancement of supersonic mixing pro-
cess if fuel is appropriately injected into these regions. Such
an analysis is planned for the near future.

Applied Magnetic Field

An external magnetic field is applied in the positive
$y-$direction. Figure 9 shows the pressure at the wall just aft
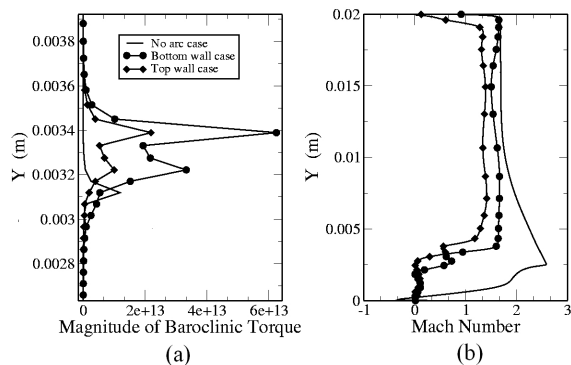of the step for various magnitudes of the applied field. The

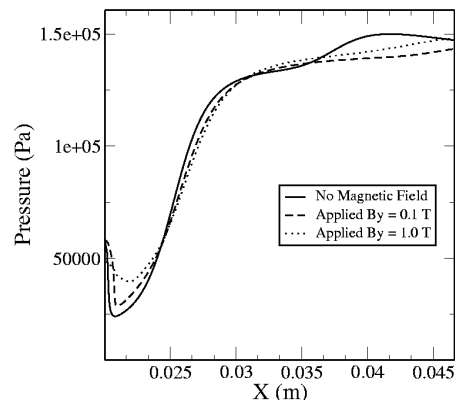Figure 8: (a) Magnitude of baroclinic torque and (b) Mach number profile in the Y-direction (10 mm from the step).

Figure 9: Pressure distribution along the bottom surface for different strengths of the external magnetic field, $\bar{B}_{ex,y} = 0.0, 0.1\ Teslas, 1.0\ Teslas$.

magnetic field increases the pressure in the recirculation region, which affects the development of the shear layer. The pressure here is the sum of the thermal pressure and the magnetic pressure given by the trace of the magnetic stress tensor. The magnetic pressure is essentially a component of the Lorentz force that acts to increase the pressure and the temperature in the recirculation zone. This result agrees with previous work (Khan and Hoffmann, 2006). It is noticed that the application of an applied magnetic field does not create any shock waves prior to the step, and thus an expansion fan is still seen at the corner.

CONCLUSION

A general-purpose MHD solve has been developed that is able to simulate supersonic MHD flow. The use of an approximate Riemann solver efficiently resolves the strong discontinuities. The plasma source generated by an electrical discharge affects the development of the shear layer. Results show that the application of external fields increases the pressure inside the recirculation zone and affects the reattachment location. By using electrical fields, significant changes in the flow features are observed, such as the formation of strong shock waves near the cathode and the anode. The shear flow that forms at the step corner no longer bends down and reattaches to the bottom wall with the magnetic field turned on. Overall, these results demonstrate the ability of the new solver to tackle problems of plasma generation in supersonic flows. Future studies will focus on applying this solver to investigate the impact of the plasma source location on fuel-air mixing and combustion in such devices.

ACKNOWLEDGMENT

REFERENCES

Cargo, P., and Gallice, G., 1997, *J. Comput. Phys.*, Vol. 136, pp. 446-466.

Einfeldt, B., Munz, C. D., Roe, P. L., and Sjogreen, B., 1991, *J. Comput. Phys.*, Vol. 92, pp. 273-295.

Evans, C. R., and Hawley, J. F., 1988, *Astro. J.*, pp. 659.

Freton, P., Gonzalez, J. J., and Gleizes, A., 2000, *J. Appl. Phys. D*, Vol. 33, pp. 2442-2452.

Gabor, T., 2000, *J. Comput. Phys*, Vol. 161, pp. 605-652.

Gurski, K. F., 2004, *SIAM J. Sci. Comput.*, Vol. 25, pp. 2165-2187.

Harten, A., Lax, P. D., and Van Leer, B., 1983, *SIAM Review*, Vol. 25, pp. 35-61.

Hartfield, R. J., Hollo, S. D., and McDaniel, J. C., 1993, *AIAA Journal*, Vol. 31, pp. 483-490.

Hsu, K. C., Etemadi, K., and Pfender, E.,1982, *J. Appl. Phys.*, Vol. 54, pp. 1293-1301.

Khan, O. U., and Hoffmann, K. A., 2006, *37th Plasmadynamics and Lasers Conference, AIAA-2006-448*.

Leonov, S. B., and Yarantsev, D. A., 2006, *44th AIAA Aerospace Science Meeting, AIAA-2006-0563*.

Li, S., 2005, *J. Comput. Phys.*, Vol. 203. pp. 344-357.

Menon, S., and Patel, N., 2006, *AIAA Journal*, Vol. 44, pp. 709-723.

Meyer, R., McEldowney, B., Chintala, N., Palm, Peter., and Adamovich, I., 2003, *41st AIAA Aerospace Science Meeting, AIAA-2003-0873*.

Miki, K., and Menon, S., 2006, *37th Plasmadynamics and Lasers Conference, AIAA-2006-2891*.

Miyoshi, T., and Kusano, K., 2005, *J. Comput. Phys.*, Vol. 208. pp. 315-344.

Patankar, S.V., 1980, *McGraw-Hill, New York*.

Schulz, J., Miki, K., and Menon, S., 2006, *37th Plasmadynamics and Lasers Conference, AIAA-2006-2894*.

Toro, E.F., 1997, Riemann Solvers and Numerical Methods for Fluid Dynamics: A practical Introduction (Springer-Verlag).

Yoshizawa, A., and Yokoi, N., 1996, *Phys. Plasmas*, Vol. 3 (10), pp. 3604-3613.